JOURNAL OF SPACECRAFT AND ROCKETS
Vol. 42, No. 5, September–October 2005

Hypersonic Experimental Facility for Magnetoaerodynamic Interactions

J. S. Shang,* R. Kimmel,† J. Hayes,‡ Charles Tyler,§ and J. Menart¶
U.S. Air Force Research Laboratory, Wright–Patterson Air Force Base, Ohio 45433

A hypersonic, weakly ionized gas experimental facility has been exclusively designed for basic research in magnetoaerodynamics. The weakly ionized air is generated by a combination of direct-current discharge, radio frequency radiation, or a combination of both in a blowdown, open-jet, Mach 5 channel. A collection of plasma diagnostic tools including optical spectroscopy, microwave devices, and Langmuir probes have also been successfully developed. The plasma field is determined to have an electron temperature around 10,000 K and the electron number density up to $2 \times 10^{12}/\text{cm}^3$. The magnetic field can be provided by a steady-state solenoid that can generate a maximum magnetic flux density up to 3 T or arrays of permanent magnets. Under this laboratory testing environment, the maximum Stuart number per unit length is around 1.5 per meter. As an example of the utility of the facility, a successful hypersonic magnetoaerodynamics experiment demonstrating the potential of a plasma actuator is described. In this experiment, the effect of an electromagnetic perturbation by a glow discharge near the leading edge is further amplified by viscous-inviscid interaction, creating a significant pressure rise over the plate surface. The induced surface pressure exhibits potential as a virtual flap for flow control.

Nomenclature

B	=	magnetic flux density
F	=	flux vectors of governing equations
L	=	characteristic dimension
p	=	pressure
S	=	Stuart number, $\sigma B^2 L/\rho u$
T	=	temperature
U	=	conservative variables
x, y, z	=	Cartesian coordinates
μ_m	=	magnetic permeability
ρ	=	air density
σ	=	electrical conductivity
$\bar{\chi}$	=	interaction parameter, $M^3(C/Re)^{1/2}$
ω_p	=	plasma frequency, $\sqrt{(ne^2/\epsilon_0 m)}$

I. Introduction

THERE is little doubt that electromagnetic-aerodynamic interaction adds a new physical dimension to aerospace vehicle performance. In particular, the Lorentz force and Joule heating introduce new mechanisms that couple directly between kinetic, thermal, and electromagnetic energy to create numerous technical possibilities for aerodynamic performance enhancement.[1,2] However, this added physical dimension is realizable only in an electrically conducting medium and in the presence of applied and induced electromagnetic fields. In hypersonic flight, the thermal excitation associated with bow shock compression can ionize air in a shock layer to create the desired flow medium. The plasma generated by thermal excitation at such a high temperature is unsustainable in a ground-testing facility. Any meaningful ground simulation therefore must rely on similitude.

Simulating a strong hypersonic magnetoaerodynamic interaction in a ground facility requires an environment in which the Stuart number $\sigma B^2 L/\rho u$ approaches or exceeds unity. This requirement is particularly severe for a weakly ionized gas generated by electron collision in a laboratory environment. The ionization process frees only outer shell electrons and occurs at the Stoletow point. According to Roth et al., the energy addition is about 81 eV per ion-electron pair of a normal glow discharge in air.[3] The ionization process by electron collision is energy efficient but also has a relatively low upper limit in electron number density.[4] From prior experience in vacuum using dc discharge, rf radiation, and electron beam, the value is generally up to 10^{13}/cc, and the electron temperature is in the range of 10,000 K (Refs. 5–7). Under these conditions, the electric conductivity of the plasma is limited to a value of 10 mho/m, an order of magnitude lower than the typical space vehicle reentry condition.[2] This shortfall therefore must be compensated by other pertinent variables of the Stuart number: the magnetic flux and air density.

Over the past few years, the plasma actuator has become the most vibrant research area for innovative flow control.[8] The basic premise is based on the interaction of a weakly ionized plasma and a strong externally applied magnetic field. However, this necessary condition might not prevail in practical applications and leads to an ineffective result. In the present effort a new approach is put forth by amplifying the relatively low-intensity electromagnetic effect by the naturally occurring viscous-inviscid interaction in hypersonic flows. Systematic research in electrode size and placement will be performed to achieve the optimal condition for strong electromagnetic and aerodynamic interactions.

For most aerodynamic applications, the typical magnetic Reynolds number is much less than unity, which implies the induced field is negligible in comparison with the applied field.[1] The applied electromagnetic field therefore will dictate the result of magnetoaerodynamic interaction. By examining the Stuart number $S = \sigma B^2 L/\rho u$, the dynamic similitude can be manipulated most effectively through the applied magnetic field intensity. At a distance much larger than the magnet size (typical for experiments using permanent magnets), the magnetic field behaves similarly to a dipole; the intensity decay is faster than the inverse cubic power to the distance from the magnetic pole. The increased intensity in

Presented as Paper 2003-0329 at the AIAA 41st Aerospace Sciences Meeting, Reno, NV, 6–9 January 2003; received 25 February 2004; revision received 7 September 2004; accepted for publication 30 September 2004.

*Emeritus Scientist and Research Professor, Wright State University, Air Vehicles Directorate. Fellow AIAA.
†Senior Research Engineer, Air Vehicles Directorate. Associate Fellow AIAA.
‡Aerospace Engineer, Air Vehicles Directorate.
§Aerospace Engineer, Air Vehicles Directorate. Associate Fellow AIAA.
¶Visiting Scientist and Associate Professor, Wright State University, Air Vehicles Directorate.

the interactive field can be achieved by increasing the magnetic field strength and by shortening the gap between magnetic poles. Meanwhile, the test section should also have a suitable dimension to allow a uniform and unperturbed stream. In the meantime, the smaller model sizes have to be compensated for by lowering the density of the wind tunnel and maximizing the applied magnetic field intensity. Last but not least, all efforts must be exercised to raise the electron number density as high as possible. From the foregoing discussions, the present effort is focused on the tradeoff of key variables to obtain the maximum Stuart number for a new low-density hypersonic plasma tunnel.

To understand this complex physics for facility development, a computational and experimental approach is necessary to describe the compact flowfield structure within the channel. The mass-averaged Navier–Stokes equations are solved to describe the detailed flowfield from nozzle settling chamber to the diffuser. Efforts are concentrated on the characteristics of the boundary layer on the tunnel wall and the free shear layer expanding into the test section. This information is used for electrode placement and for determining the size of the hypersonic inviscid core. All data will be validated by redundant measurements or comparison with calculations whenever possible.

II. Experimental Facility

The hypersonic low-density tunnel is a basic blowdown, free-jet facility. The rectangular cross-section, conical nozzle with a throat area of 73.4×5.08 mm expands to the nozzle-exit plane of 73.4×177.8 mm. It is designed to deliver a nominal Mach 5 source flow in the test section. The test section currently in use has the dimension of $177.8 \times 228.6 \times 73.4$ mm ($L \times H \times W$). The diffuser is designed to achieve at least normal shock recovery, and the entire length of the tunnel is 1555 mm. To avoid unintentional grounding, the facility is constructed of Plexiglas®. For nonintrusive diagnostic measurements, two 235-mm-diam quartz windows were mounted on the side walls of the test section. The window exposes the entire test section including the nozzle-exit plane. A sketch of this plasma channel is presented in Fig. 1. Dry air is supplied from the facility bottle farm through a three-stage pressure-reduction system. The tunnel exhausts to a 2800-m^3 vacuum sphere.

The simulated altitude range (based on static density) of the new facility extends from 30,000 to 50,000 m (100,000 to 150,000 ft). At a fixed stagnation temperature of 300 K, the tunnel has an operational stagnation pressure range from 0.1 to 1.0 atm, and in this pressure range the airstream is free from condensation.[9] At a stagnation pressure of 300 torr, the freestream in the test section has a velocity, density, and temperature of 698.4 m/s, 0.005 kg/m^3, and 51.6 K, respectively. Under these conditions the mass-flow rate is 0.046 kg/s, and the unit Reynolds number in the test section is 1.15×10^6 per meter.

The relatively shorter span between the tunnel sidewalls compared to the vertical dimension is designed to achieve the maximum transverse magnetic field strength by narrowing the gap between the poles of magnets. Meanwhile, this construction also must maintain an inviscid core in the test section. From the basic rectangular nozzle and diffuser configurations, the available uniform flowfield for testing is confined within a rhombohedron. The leading surfaces of this uniform flow region are bounded by the expanding freejet; the trailing surfaces are bounded by the coalescing shocks that originate from the reflection to the free pressure surface in the test chamber. The maximum testing cross section is estimated to be 38×150 mm immediately downstream of the nozzle exit. This physical dimension also limits the size of model that can be tested before blockage significantly alters the flowfield.

Another unique feature of the Mach 5 tunnel is the low-density environment. To achieve a strong magnetoaerodynamic interaction, the plasma channel is design to operate at a stagnation pressure range from 0.1 and 1.0 atm. Under these conditions, the air density in the inviscid core spans a range from 0.0013 to 0.013 kg/m^3, and the neutral particle number density is 3×10^{16} to 3×10^{17} per cc. As a consequence the mass-flow rates vary from 0.007 to 0.13 kg/s, and a continuous operation can be easily sustained.

A three-dimensional traverse mechanism was also developed for the facility for flowfield probing. This mechanism has a freedom of movement to cover the entire domain of the test section ($177 \times 152 \times 73$) mm. The placement of the traverse is controllable within a distance of 0.25 mm. All experimental data were collected by an HP 3852A data-acquisition and control system. For flow visualization, a single-pass schlieren system with an arc lamp light source and a high-speed video camera were originally used.[10] This system has been updated to use pulsed light source including light-emitting diodes, a Xenon Corp Model 437-B Nanopulser™ spark source, or laser breakdown to provide high-resolution imaging in conjunction with a 10-bit charge-coupled-device camera.[10,11]

III. Plasma Generation

The air plasma in the present hypersonic channel is generated by dc gas discharge, rf radiation, or a combination of both. In previous efforts to measure plasma properties in a vacuum chamber,

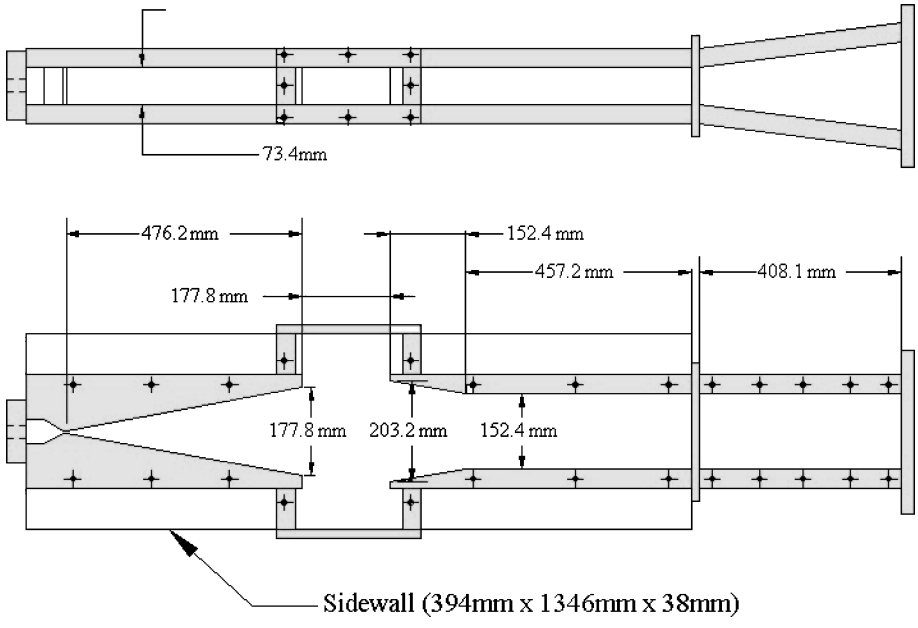

Fig. 1 Sketch of Mach 5 plasma channel.

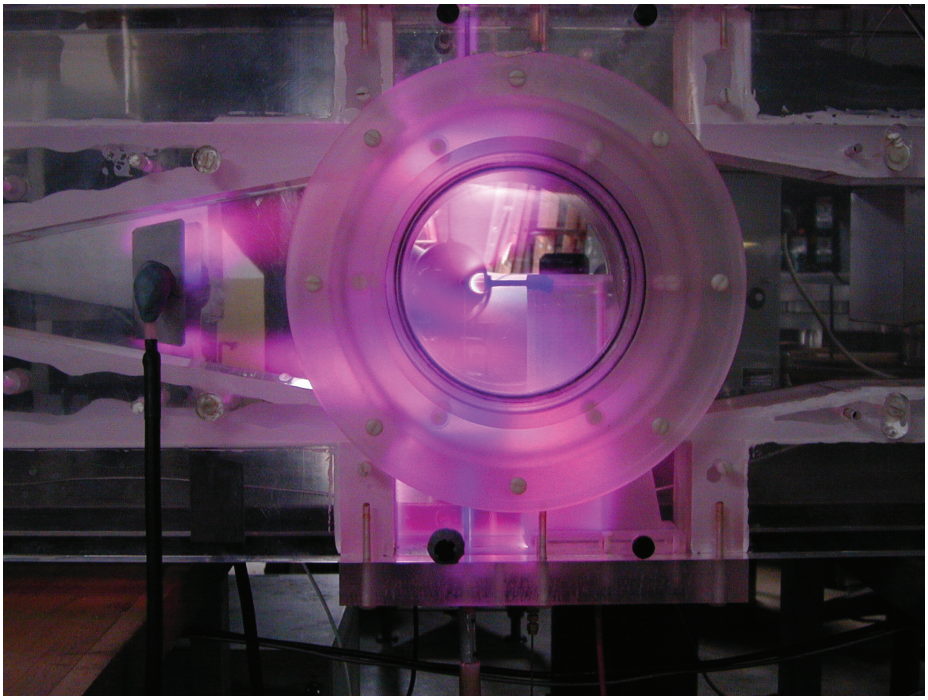

Fig. 2 RF discharge in the Mach 5 plasma channel.

the impedance of the dc discharge was reduced by a factor nearly two by adding rf radiation to the plasma generation.[12] In short, rf radiation was effective in enhancing the dc discharge in a vacuum chamber even at a static pressure as high as 7 torr. To overcome the principal loss from the attachment processes, both from the ground state and metastable molecules, the dc and rf discharges might have to operate simultaneously to increase the charged particle density.

The combined dc and rf operation in the tunnel offers wide flexibility depending on the test objective. In one of these arrangements, rf antennas with a thickness of 0.05 mm are attached to the sidewall and placed 279.4 mm downstream from the nozzle throat. The two trapezoidal antennas have a surface area of 3266 mm^2 each and are made of polished brass. Numerical simulation indicates a hydraulically smooth surface for roughness less than 0.12 mm; thus, the effect of the antennas thickness on the flow is expected to be negligible. Shakedown runs of the facility verified this assessment. The most efficient application of plasma generation is to take advantage of the high electron number density immediately adjacent to the electrode. In this arrangement, the highest electric conductivity of the medium will concentrate very close to the wall where an externally applied magnetic field also retains maximum intensity.

The dc discharge is provided by a group of Universal Voltronics BRC-10-1000R-STD-3PH-208V reversible polarity switching power units. One of the units is rated at 8 kW with 10-kV output at a signal impedance of $10 \times 10^3\ \Omega$. At the breakdown voltage of 400 V, a diffuse discharge was achieved at a plasma current as high as 550 mA. The discharge changes into multiple streamers when the electrical current exceeds 900 mA. Other dc power supply units are also available. They are rated at 4 kW with 10-kV output source at the same signal impedance. The maximum current output however is limited to 400 mA.

The rf power supply and its automatic matching network are the Dressler CESAR-1350 and VM5000W, respectively. This integrated unit is water cooled and can deliver up to 5 kW at 13.56 MHz into a 50-Ω load. In fact, the rf plasma generation is not treated as an antenna problem but as a rf-carrying electrode with an ambient ground plane. In routine operation, the automatic matching network will keep the reflected power to less than 2%. Figure 2 depicts the weakly ionized gas generated by the sidewall-mounted rf antenna. Although a high concentration of charged particles was detected in the relatively low-density region of the shear layer, the plasma generation process can still be enhanced by a glow discharge on a model surface. In summary, the energy required for plasma generation in this facility is extremely limited. A typical value less than 2 kW is needed to sustain its operation.

IV. Applied Magnetic Field

A key element in simulating the magnetoaerodynamic interaction in flight is the strength of the applied magnetic field. Based on the Stuart number, the low electron number density in the ground-testing facility must be compensated by the applied magnetic field strength B. In fact, it is also the most effective control parameter because the interaction parameter is increased according to the square power of the magnetic field intensity. In the present facility, the transverse magnetic field can be generated by a steady-state solenoid or an array of neodymium rare-Earth (NdFeB) permanent magnets.

The principal external magnetic field generator is the GMW 3474 electromagnet. This system is a continuous-operation, water-cooled model. The coils, when connected in series, have a maximum power rating of 10.6 kW (140 A, 76 V). Pole spacing is adjustable from 1–160 mm, and pole cap diameters range from 25–250 mm. Field strength is a function of pole gap and pole-cap diameter. With a pole gap of 10 mm and pole diameter of 25 mm, the field strength is as high as 3.5 T. In practice, the magnet for the plasma channel is always operated at the maximum pole spacing and pole-cap diameter to clear the channel sidewalls. Under these conditions, the transverse magnetic field has a magnitude of 1 T and is nearly uniform. The magnet is rail mounted so that it can be moved downstream to access the test section.

In case a magnetic field is needed immediately adjacent to the small model surface, compact neodymium rare-Earth permanent magnets can be very attractive.[12] The NdFeB magnet has a higher maximum energy product $(BH)_{\max}$ than other rare-Earth permanents. These magnets are commercially available in a wide variety of shapes and sizes. At the pole surface the magnetic field strength is greater than 0.47 T. A weakness of the NdFeB permanent magnet in comparison with the aluminum-nickel-cobalt alloy (Alnico) is the much lower Curie temperature; therefore, the maximum working temperature for NdFeB is 180°C. This shortcoming is not overly detrimental for most of the testing conditions within the present facility.

Based on the known applied magnetic field strength and the electrical conductivity of the generated air plasma, the Stuart number per

unit characteristic length $\sigma B^2/\rho u$ in the present facility is estimated around 1.5. This value is determined by the electrical conductivity σ of 10 mho/m. However, the present experimental experimental effort has demonstrated that the externally applied magnetic field need not be dominant if the magnetoaerodynamic perturbation is further amplified by a subsequent viscous interaction.

V. Diagnostic Capability

A critical element of the present effort is the development of diagnostic capability for determining properties of a weakly ionized gas. Several properties are important for a magnetoaerodynamic experiment, one group of them being the temperatures of various internal degrees of freedom. These data describe the distribution of possible species concentration and the energy state of the gas mixtures. The other group of properties include the electrical conductivity, electron, and ion number density. These data are intrinsic properties of the plasma and are measured by a combination of direct and nonintrusive techniques.

The gas mixture temperature measurement is obtained from the spectrum measurement in the second positive electronic transition of nitrogen from $C^3\Pi_u$ to $B^3\Pi_g$ (Ref. 13). The spectrum measurement system is developed by Research Support Instruments, Inc. The system hardware consists of a fiber-optic probe connected to the Ocean Optics PC 2000 spectrometer. A collimating head can be attached to the fiber-optic probe to improve spatial resolution. Temperature is determined via the Boltzmann plot method. The logarithms of relative intensities of the transitions are plotted vs wave number. Vibrational temperatures are extracted from the slope of the curve-fitted results. Rotational lines are not fully resolved by the spectrometer, so that rotational temperatures are estimated comparing a simulated spectrum to the measured spectrum. Twenty rotational lines are simulated at each of 15 vibrational transitions. The predicted spectrum is convolved with the slit function of the spectrometer, and the mean square error between the predicted and measured spectrum is computed. This curve-fitting procedure is done in 10-K increments, effectively creating a 10-K resolution in the measured temperature. The system and data analysis are described in more detail in Ref. 11.

Typical rotational and vibrational temperature measurements in a dc discharge electrode arrangement are given in Figs. 3 and 4. The dc discharge is maintained between two flat-plate electrodes, 46 mm in length along the streamwise direction and 6 mm wide in the spanwise direction. The probe was located on the centerline of the electrodes and 32 mm downstream from the leading edge of the electrodes. The data were collected for the discharge current from 50 to 400 mA. At this location, the error bar ($\pm 1\sigma$) in the measurement reflected the unsteadiness of the plasma at the higher discharge current (400 mA).

In Fig. 3, the rotational temperatures at the centerline of the channel range from approximately 70 K for the 50-mA current to near

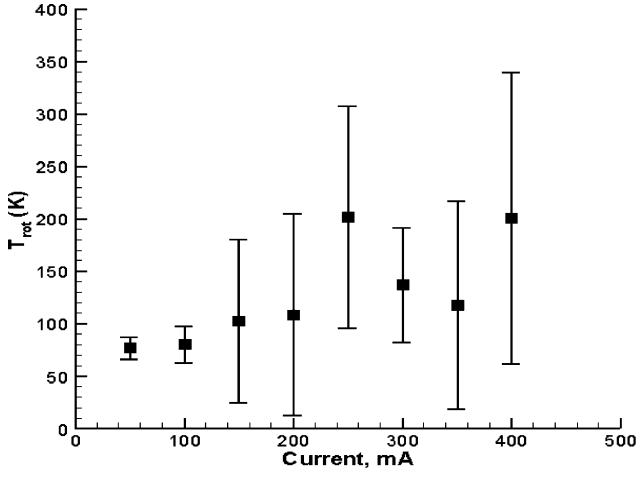

Fig. 3 Rotational temperature vs dc discharge electrical current: *Po* = 370 torr, *To* = 300 K, and *E* = 1.2 kV.

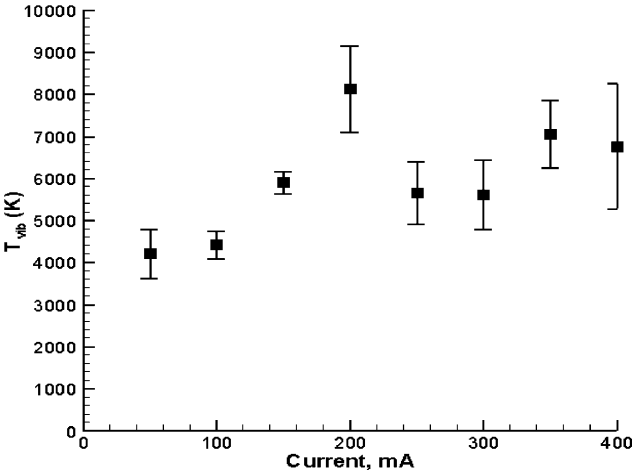

Fig. 4 Vibrational temperature vs dc discharge electrical current: *Po* = 370 torr, *To* = 300 K, and *E* = 1.2 kV.

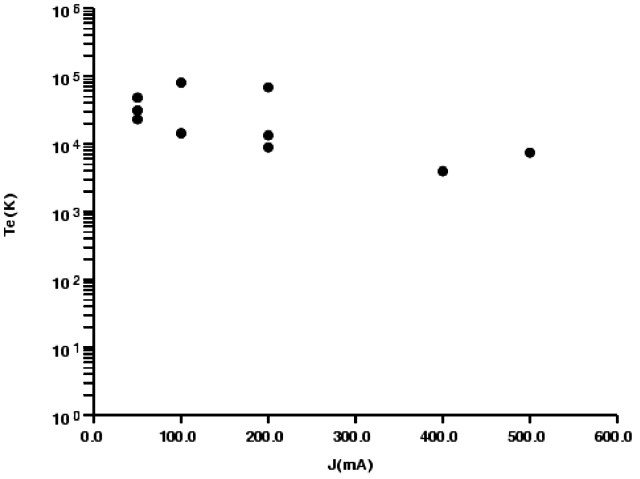

Fig. 5 Electron temperature vs dc discharge electrical current: *Po* = 370 torr, *To* = 300 K, and *E* = 1.2 kV.

200 K for the 400-mA discharge current. The measured rms value of temperature above 100 mA indicates a significant unsteadiness. At the extreme limit of abnormal glow discharge, the measured rotational temperatures show an increasing trend with an increasing discharge current. In Fig. 4, the vibrational temperature distribution with respect to the discharge current is given. The vibrational temperatures span a range from 4000 K at a discharge current of 50 mA to 7000 K at 400 mA. Beyond a discharge current of about 200 mA, the vibrational temperature appears to saturate around 5000 to 7000 K. Pitot-probe measurements in the discharge show little change compared to no-discharge values, indicating that the energy cascade to translational temperature is negligible in the bulk of the glow.[11]

A sustained development of a double Langmuir probe has been successfully carried out by Menart et al.[14] This probe is constructed of a twin 0.2-mm-diam platinum wire embedded in a ceramic sleeve with a separation distance of 0.5 mm. The sleeve covers all but 1.27 mm from the tip of the wires; thus, the sensing area for each wire is 0.83 mm^2. A Keithly 230 bipolar power supply with 100 programmable channels having a ± 100 V range with ± 100-mA current limit powers the probe.

A series of Langmuir-probe measurements of discharges from dc rod electrodes with a gap distance of 50 mm were taken. The data depicted in Figs. 5 and 6 were collected adjacent to the vertical centerline between electrodes and the test section. In general, the electron temperature measurements agree very well with the data from an optically pumped plasma.[15] In Fig. 5, the measured electron temperatures are presented over the entire discharge current range.

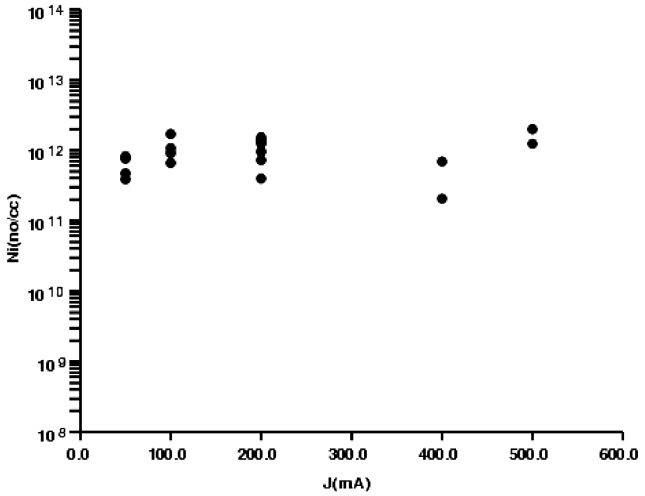

Fig. 6 Ion number density vs dc discharge electrical current: *Po* = 370 torr, *To* = 300 K, and *E* = 1.2 kV.

The data scatter of the electron temperature reflects the unsteady behavior in the abnormal glow discharge domain. Nevertheless, the electron temperature distribution lies in the range from 10^4 to 10^5 K.

The measured ion number density distribution is given in Fig. 6. These data were collected from the rod-electrode arrangement for discharge currents up to 500 mA. An average value over the entire measured range is around 2×10^{12}. From the measurements, the mean free paths of the electrons and ions are determined to be around 150 and 30 μm, respectively. The Debye length is about 70 μm. These characteristic lengths associated with the probe put the measuring environment in the transitional regime.[16,17] However, some of the data scattering are incurred by the rather thin discharge domain between the rod electrodes, which can be improved by different electrode shape.

Nonintrusive plasma diagnostics for the plasma channel are based on the dispersive property of microwaves propagating in a plasma.[18] The basic measuring system consists of a Roscoe Microwave generator with a detector, an HP 5340 Microwave frequency counter, and two sets of horn antennas. The microwave generator has a frequency range from 10 to 18 GHz, at a maximum output of 14.9 dbm (31 mW). The detector has a sensing upper limit of -25 dbm (0.034 mW). This system therefore can measure an electron number density up to about $10^{13}/\text{cm}^3$ with a spatial resolution of 42 mm. A series of tests was carried out to determine the peak power obtainable from different separation distances between transmitting and receiving horns. The detailed description for all plasma diagnostic tools for the Mach 5 channel can be found in the two accompanying reports by Menart et al.[16] and Menart and Shang.[17]

In the present effort, it is determined that the charged particle number density can be measured within a factor of 3 in the tested range ($10^{12}/\text{cm}^3$). The greatest uncertainty in these results comes from flowfield interference to the data collecting process. This result reflects the current state of the art of Langmuir probes in determining transport properties of plasma in a hypersonic stream.

VI. Numerical Analysis

To verify the design flowfield characteristics and provide a detailed electrode placement analysis, a numerical analysis for the complete Mach 5 channel was performed. The numerical simulation needs to describe the flowfield starting from the nozzle throat until far downstream of the diffuser. The diffuser is designed for a normal shock recovery; thus, a strong shock-wave boundary-layer interaction is anticipated in the computational domain. The numerical simulation is obtained by solving the mass-averaged, time-dependent, three-dimensional Navier–Stokes equations. This system of equations is solved by an implicit, time-accurate, unstructured Euler/Navier–Stokes solver, Cobalt.[19] The numerical algorithm is based on the Riemann formulation of Gottlieb and Groth[20] and implicit time stepping to yield second-order spatial and temporal accuracy. The second-order spatial accuracy is achieved by the least-squares total-variation-diminishing scheme in the flux reconstruction process. The viscous flux vectors are formulated to satisfy the discrete maximum principle that guarantees conservation and yields a linearity preserving discretization. The neighbor-cell connectivity of an unstructured grid formulation greatly enhances an exceptionally scalable, parallel computing performance when this numerical procedure is ported to multicomputers using a message-passing-interface library.[21]

The mass-averaged Navier–Stokes equations in integral form are written as follows:

$$\frac{U}{t}\iiint U\,\mathrm{d}v + \iint \left(F_x^+ + F_x^- + F_y^+ + F_y^- + F_z^+ + F_z^-\right) \times n\,\mathrm{d}s + \iint \left(F_{x,v}^+ + F_{y,v}^- + F_{z,v}\right) \times n\,\mathrm{d}s = 0 \tag{1}$$

where F_x^+, F_x^-, F_y^+, F_y^-, F_z^+, and F_z^- are the split flux vectors derived from the inviscid terms. $F_{x,v}^+$, $F_{y,v}^-$, and $F_{z,v}$ are the flux vectors of the viscous terms in the governing equations.

The governing equations are discretized by the fully implicit numerical scheme as

$$[3(U^{n+1} - U^n) - (U^n - U^{n-1})]/2\Delta t + \nabla \cdot F = 0 \tag{2}$$

where the U are the conservative independent variables $U(\rho, \rho u, \rho v, p)$. The reconstruction of the flux vectors at the centroid of the cell faces is by a least-square solution to the following approximation:

$$U_{i\pm\frac{1}{2}} = U_i \pm \bar{r} \cdot \nabla U_i \tag{3}$$

where $U_{i\pm 1/2}$ are the reconstructed left and right side of the variables at the cell interface and ∇U_i is the gradient vector for the cell i.

In the present application, the no-slip velocity components and the constant temperature condition are imposed on the flow channel walls. The surface density value is then obtained by the zero-normal-pressure-gradient approximation, $\bar{n} \cdot \nabla P = 0$. The sonic throat condition is specified at the upstream boundary, and the no-reflection condition and a prescribed reservoir pressures are used at the far downstream of the diffuser. Turbulent closure is achieved by the Spalart–Allmaras one-equation model.[22]

The entire flowfield of the Mach 5 channel is simulated by a three-dimensional mesh system of 1,665,104 cells. At any given streamwise cross section, the flowfield is resolved by no fewer than 8000 cells. The finest cell spacing adjacent to the solid surface is maintained in the law-of-the-wall variable to the order of magnitude of unity, $2.08 \le y^+ \le 3.24$. The numerical result is obtained for the stagnation pressure of 300 torr and stagnation temperature of 300 K, respectively. To ensure a stable and converged numerical result, the far downstream pressure is set to be lower than the vacuum sphere, 2.5 vs 8 torr.

The numerical result verifies the design condition; indeed, a Mach number of 5.09 inviscid core is achieved at the nozzle exit, and the flow is continually expanded downstream and reaches a maximum Mach number of 5.27 at a distance 102 mm farther downstream. From the numerical simulation, the boundary-layer thickness on the channel sidewall is determined to be 12 mm, so that the usable inviscid core at the nozzle exit is around 50 mm. All this detailed flowfield structure can be discerned in Fig. 7, a closeup side view of the computed density contour. The most predominant feature is the coalescing shock waves in the test section that originated at the trailing edge of the nozzle. These shock waves are further reinforced by the diffuser downstream. The available rhomboidal uniform inviscid core can be slightly enlarged by a higher stagnation pressure condition.

High parallel computing efficiency is also clearly demonstrated by Cobalt. The data-processing rate is 2.81×10^{-5} seconds per cell per time step on a 30-node configuration of the U.S. Air Force Research Laboratory/VA Beowulf computer cluster. All numerical

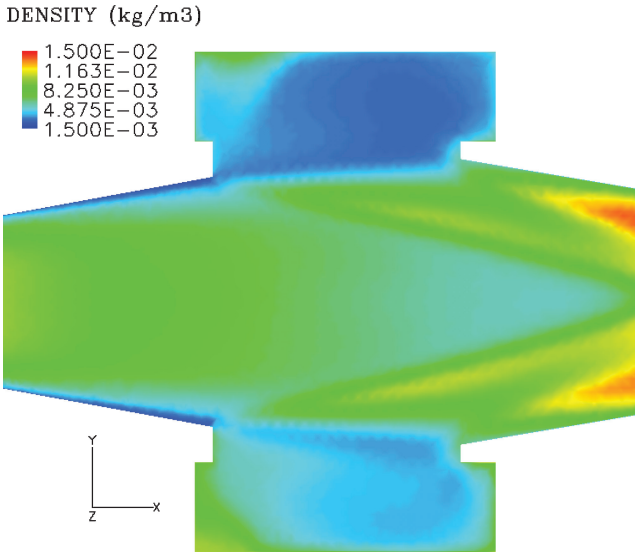

Fig. 7 Density contours in test section: *Po* = 370 torr, and *To* = 300 K.

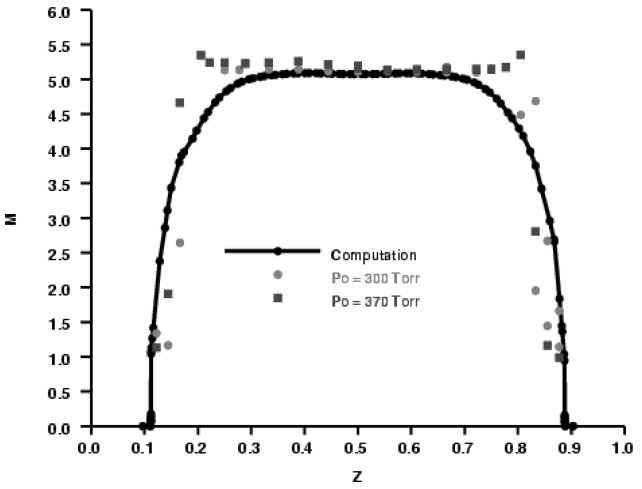

Fig. 8 Vertical Mach-number profile at nozzle exit.

results presented have reached a steady-state asymptote after about 7000 time steps.

VII. Flowfield Survey

At the present low-density freestream condition, a high-resolution schlieren image faces severe technical challenges. For the present, the flowfield structure is determined by a pitot-probe survey. All data were collected by a single pressure transducer. The Baratron MKS model 722A-23320 absolute pressure gauge has a calibrated accuracy of ±0.1% of the 100-torr full range. The flowfield structure in the test section is described by traversing the probe at three streamwise locations: the nozzle-exit plane, 50.8 mm, and 101.6 mm downstream. In the present effort, data were collected for three stagnation pressure conditions: 300, 370, and 460 torr. At each stagnation pressure, survey data were collected in the center plane at different elevations and across the span of the test section at three streamwise locations. The accompanying numerical simulation, however, is limited to the lowest stagnation pressure condition.

Figure 8 presents Mach-number profiles on the channel centerline at the nozzle exiting plane. These Mach-number profiles are deduced from the Rayleigh pitot pressure formula at different vertical locations. These data were collected at a stagnation temperature of 300 K and the stagnation pressures of 300 and 460 torr, respectively. Under these conditions, the inviscid core has a dimension more than 107 mm in the z coordinate irrespective of the different stagnation pressures. At the lower stagnation pressure the deduced

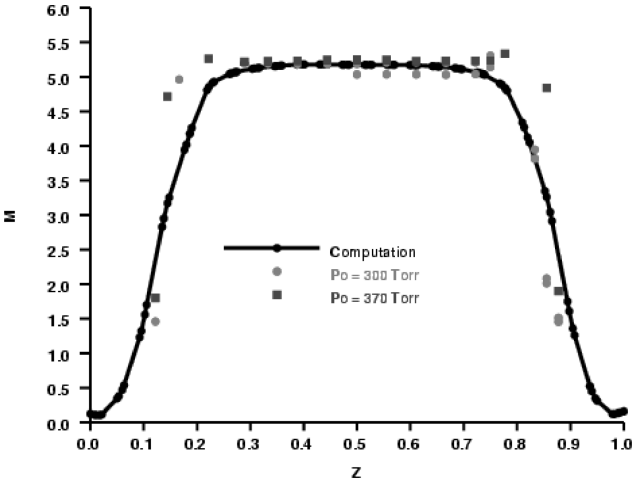

Fig. 9 Vertical Mach-number profile at 50.8 mm downstream of nozzle exit.

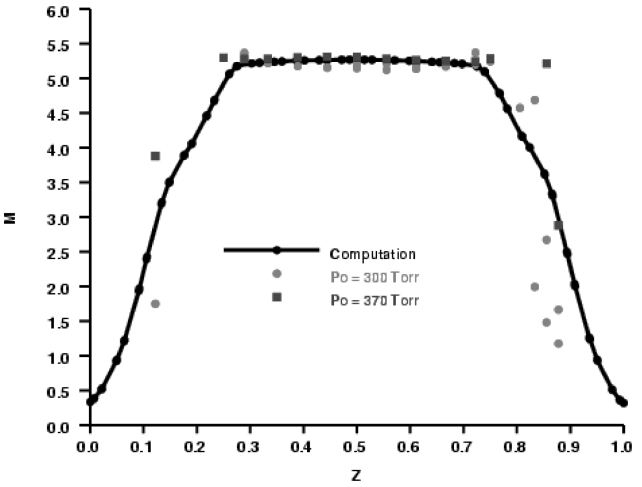

Fig. 10 Vertical Mach-number profile at 101.6 mm downstream of nozzle exit.

Mach profile has an average value of 5.14. At the higher stagnation pressure, the core Mach numbers are clustered around 5.22. These data are in good agreement with the numerical result both in the Mach number (5.09) and core size.

The Mach-number profiles at a distance of 50.8 mm downstream from the nozzle exiting plane are depicted in Fig. 9. At this location, the computed Mach distribution is bracketed by the data from two different stagnation pressure conditions. The Mach-number data exhibit a scatter from 5.03 to 5.23, and the computed result shows a value of 5.19. Equally important, the measured and computed inviscid core also show a good agreement. The last survey station at a distance of 101.6 mm downstream of the nozzle-exit plane is given by Fig. 10. At this survey station, the computed result is again bracketed by the measured Mach numbers that exhibit a scatter from 5.12 to 5.28. The higher measured values correspond to the higher stagnation pressure condition. The numerical result indicates a value of 5.27 in the inviscid core along the vertical or the Z coordinate.

Figures 11–13 depict transverse pitot-pressure surveys across the span of the test section at the three streamwise locations: the nozzle-exit plane, 50.8 mm (Fig. 12), and 101.6 mm (Fig. 13) downstream. Data were collected at stagnation pressures of 300 and 370 and three different elevations (the plane of symmetry, $z = 0.0$ and ±38.1 mm). In the range of Reynolds numbers tested, data sets indicate a sidewall boundary-layer thickness about 7 mm beneath a weak shock.

Experimental and computational results reveal a diminished inviscid core downstream bounded by a weak oblique shock. The disparity between experiment and computation in the outer portion of the free shear layer arises because the pitot data were reduced

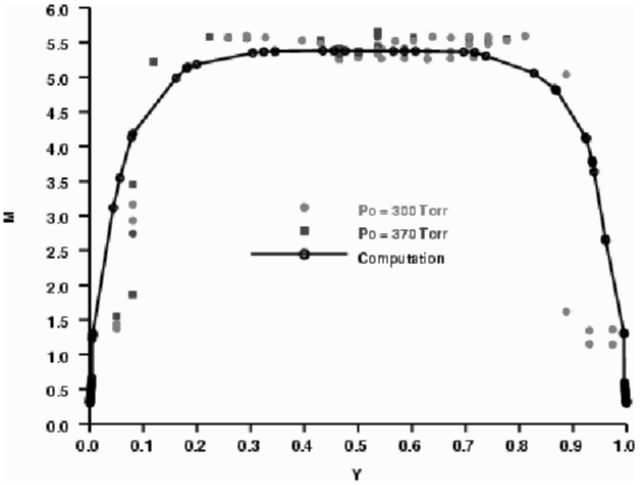

Fig. 11 Transverse Mach-number profile at nozzle exit.

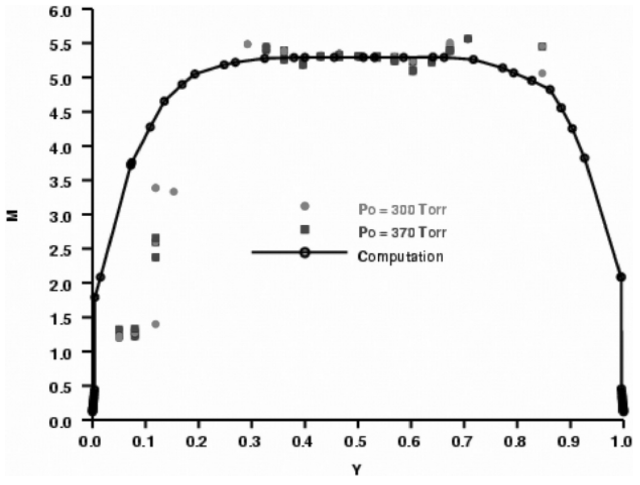

Fig. 12 Transverse Mach-number profile at 50.8 mm downstream of nozzle exit.

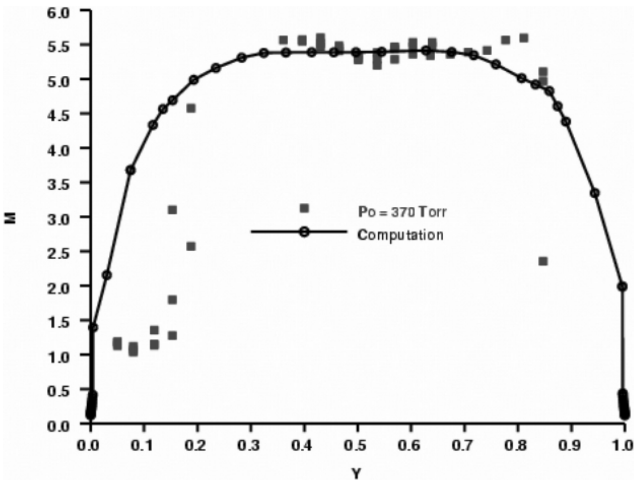

Fig. 13 Transverse Mach-number profile at 101.6 mm downstream of nozzle exit.

using the freestream static pressure, rather than the local static pressure behind the weak wave at this location, leading to a spuriously high Mach number. For the present purpose, the comparison between experimental and computation indicates that a sizable unperturbed inviscid core exists for experiments.

From the numerical result and pitot-probe survey, the axial gradient of the source flow is essentially negligible in the test section. Figure 14 presents the Mach-number distributions at two stagnation pressures along the centerline of the channel. At a stagnation pressure of 300 torr, the usable inviscid core is shortened to 80 mm by the diffuser shocks. At the normal operating stagnation pressure of 370 torr, the Mach number ranges from the value of 5.35 at the nozzle-exit plane to 5.43 at a distance of 50.8 mm and finally to 5.67 at the farthest survey station downstream. The centerline Mach number varies by less than a value 0.07 over the distance of 100 mm or less than 2%. This aerodynamic quality is remarkable for a channel of this small dimension.

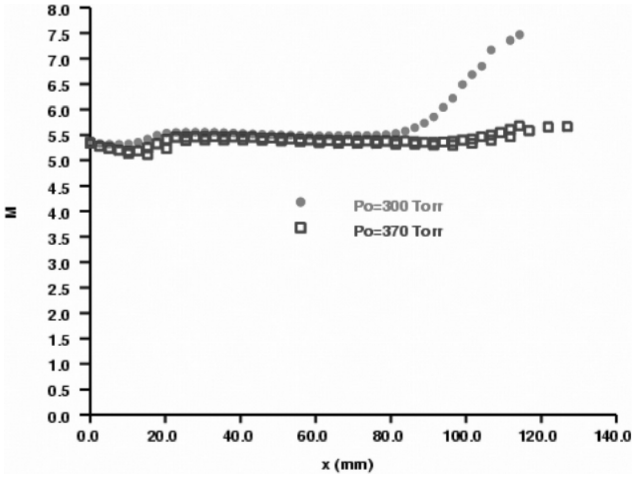

Fig. 14 Mach-number distribution along channel centerline.

The combined survey data reveal a uniform 100×50 mm inviscid core extending a distance of 120 mm from the nozzle-exit plane downstream. This survey also verifies the estimate that the admissible roughness height near the nozzle exit is around 0.13 mm. This information is critical for the placement of either the dc or the rf electrodes for plasma generation. A single-pass schlieren system was used to assess the flowfield quality. The experimental observation substantiates the survey data of a shock-free flowfield in the test section. Although the core size of the low-density tunnel is rather limited, the flow quality in terms of low streamwise gradient is excellent.

VIII. Magnetoaerodynamics Interactions

As the consequence of huge ionizing energy requirements, most magnetoaerodynamic experiments performed in legacy ground facilities are severely limited to plasma with low electrical conductivity.[1,4,7] To simulate a measurable magnetoaerodynamic interaction, the experiment either must introduce seeding material into the flow medium or apply a strong magnetic field. Recently, actuators using electromagnetic force alone have become the most active research area for plasma flow control. In most applications, electron collision is adopted as the principal plasma generation mechanism. The plasma generated by the process has an upper limit of electron number density around 10^{12}/cc, and the electrical conductivity is generally lower than 10 mho/m. Therefore, the magnetoaerodynamic interaction can only exhibit a modest modification to the entire flowfield.[4,5,7]

From electrodynamics research using the drift-diffusion model, it was found the electron number density is an order of magnitude higher in the cathode region than the positive column.[23–25] From numerical simulations, it was further noticed that the charge separation occurred over the electrodes and immediately above the plasma sheath.[23] In the near-surface region, a strong magnetic field can be maintained with minimum energy input. This phenomenon is favorable for hypersonic magnetoaerodynamic interaction, because any small perturbation to the displacement of the shear layer near the leading edge will induce a strong pressure interaction.[26] In fact, the induced pressure rise is proportional to the cubic power of the freestream Mach number, $\bar{\chi} = M^3(C/Re)^{1/2}$. By integrating the electromagnetic perturbation to the shear-layer structure with further amplification by the viscous-inviscid interaction, an induced surface-pressure rise over a substantial region can be significant.

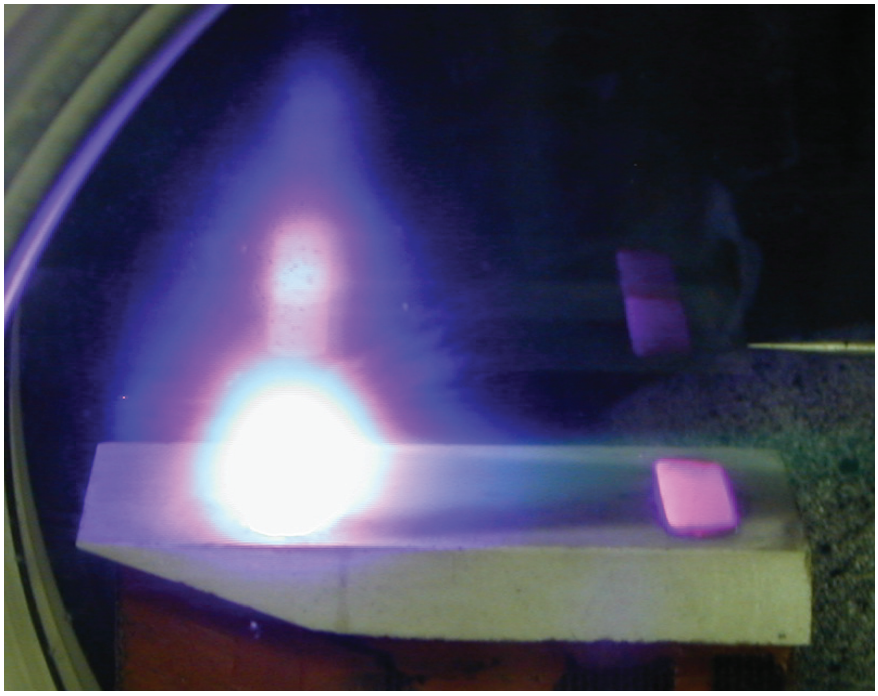

Fig. 15 DC glow discharge over model in hypersonic magnetohydrodynamics channel: $Po = 370$ torr, $To = 300$ K, $B = 0$, and $E = 1.2$ kV.

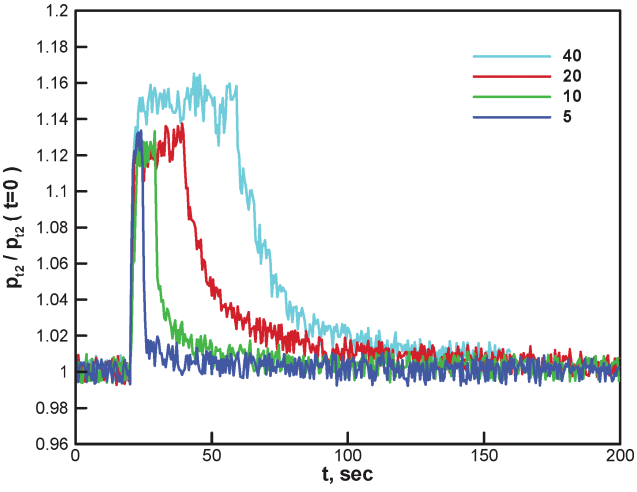

Fig. 16 Time traces of surface pressure by magnetoaerodynamic interaction: $Po = 370$ torr, $To = 300$ K, $B = 0$, $E = 1.2$ kV, and $J = 50$ mA.

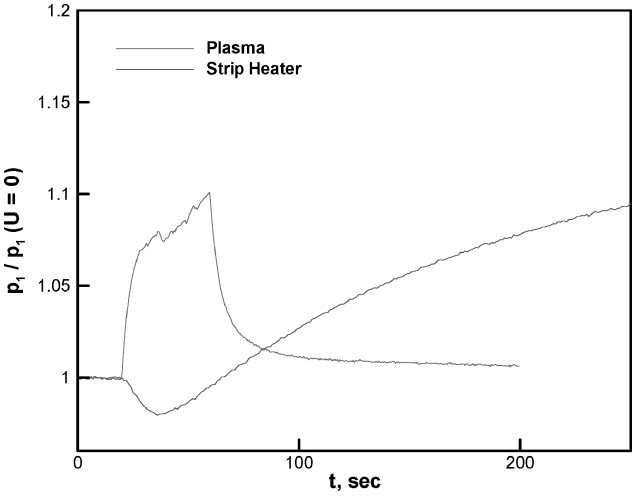

Fig. 17 Compare surface-pressure data by joule and electrode heating: $Po = 370$ torr, $To = 300$ K, $B = 0$, and $PW = 60$ W.

These observations open a new avenue for hypersonic plasma actuators for flow control.

To test this idea, electrodes for a dc glow discharge with a span of 31.75 mm are embedded on a flat-plate model. The cathode is placed 19 mm downstream and parallel to the leading edge, and the anode is 38.1 mm farther downstream. Figure 15 shows the glow discharge ignited at a power of 60 W (50 mA at 1200 V). The glow is more pronounced over the cathode than anode. The electron number density in the discharge region was less than 10^{12}/cc, and the maximum (steady-state) electrode temperature is about 520 K. The experiments were conducted without an externally applied magnetic field, and so the major contributor to the modified shear-layer structure is Joule heating. As a secondary evidence of the volumetric heat addition, the air temperature adjacent to electrodes was actually greater than the surface electrode temperature.

Three pressure taps were installed on the model. These measurements indicated that the Joule heating alters the growth rate of the shear layer, and this change is amplified by the classic pressure interaction to produce a pressure plateau over the plate. In Fig. 16, the pitot pressure above the anode is presented for different periods of plasma ignition, from 5 to 40 s. The flowfield responds to the plasma turn-on in a time less than or equal to the probe response time, which was measured to be 1 s (Ref. 25).

To ascertain that the observed magnetoaerodynamic interaction truly was via Joule heating, the cathode was replaced by a resistance heater and supplied with the same amount of energy (60 W). In Fig. 17, the surface-pressure response from the Joule heating and convective heating are depicted side by side. It is clearly demonstrated that the induced pressure by volumetric Joule heating is dominant over that by convective heating at the onset of measurements. The response of the plasma actuator is also orders of magnitude faster than the convective heating alone. For a flow control device, this attribute is highly desirable. The key point of this comparison is that the plasma actuator is a genuine magnetoaerodynamic interaction.

The pressure increment over the classic viscous interaction pressure is 8% at a power of 60 W, and the value increases with an increased power input.[24,25] In Fig. 18, the surface-pressure

measurements for a range of power supplied to the glow discharge (60–350 W) are presented with the classic theory of viscous-inviscid interaction.[26] The data were collected in the absence of an externally applied magnetic field, $B = 0$; therefore, the principal effects are contributed by the volumetric Joule and convective electrode heating. The surface-pressure rise is generated by the electromagnetic perturbation of the boundary-layer displacement thickness growth rate and further amplified by the viscous-inviscid interaction. This resultant surface pressure is greater than the classic hypersonic viscous interaction.[26] As a measure of the effectiveness of the plasma actuator, the modified pressure can be compared to that generated by a deflected control surface. Oblique shock calculations show the equivalent control surface deflection increases from the 1.1 to 3.6 deg as the discharge power increases from 60 to 350 W. The energy scale for this hypersonic plasma actuator is 1.89 W/deg · mm.

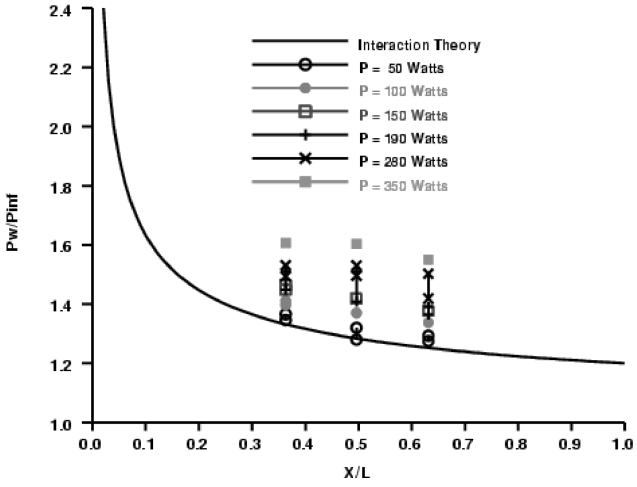

Fig. 18 Surface-pressure distributions vs glow discharge power supply: $Po = 370$ torr, $To = 300$ K, $B = 0$, 60 W < PW < 350 W.

Additional experiments with an externally applied magnetic field including the Lorentz force and Hall effects have revealed a greater complexity and even greater application potential.[24,25] Figure 19 presents the composite depiction of the glow discharge behavior in an applied external magnetic field. The upper-most image shows the side view of a glow discharge in the absence of an applied magnetic field, $B = 0$. The glow emission is most pronounced over the cathode, and the discharge domain is located over the plate surface between electrodes. When a magnetic field of 1 T is applied in such a polarity that the resultant Lorentz force is pointed upward from the plate surface (middle image, $J \times B > 0$), the most outstanding feature is that the applied magnetic field suppresses the mobility of charged particles. In spite of the fact that the Lorentz force accelerates the charged particles away from the plasma sheath region, they are constricted by the strong magnetic force. The glow intensity is seen to diminish over the region immediately adjacent to the plate surface between electrodes. By reversing the magnetic polarity, the Lorentz force is counteracting the Joule heating effect for increasing the boundary-layer displacement thickness (Bottom image $j \times B < 0$). The added complexity of the Hall effect and ion slip in a partially ionized gas require more efforts for a better understanding.[24,25] A continuing side-by-side experimental and computational research is presently sustained.

These experimental data clearly show that the hypersonic plasma actuator indeed brings an expanded physical dimension to flow control. Taking the idea a step further, the magnetoaerodynamic

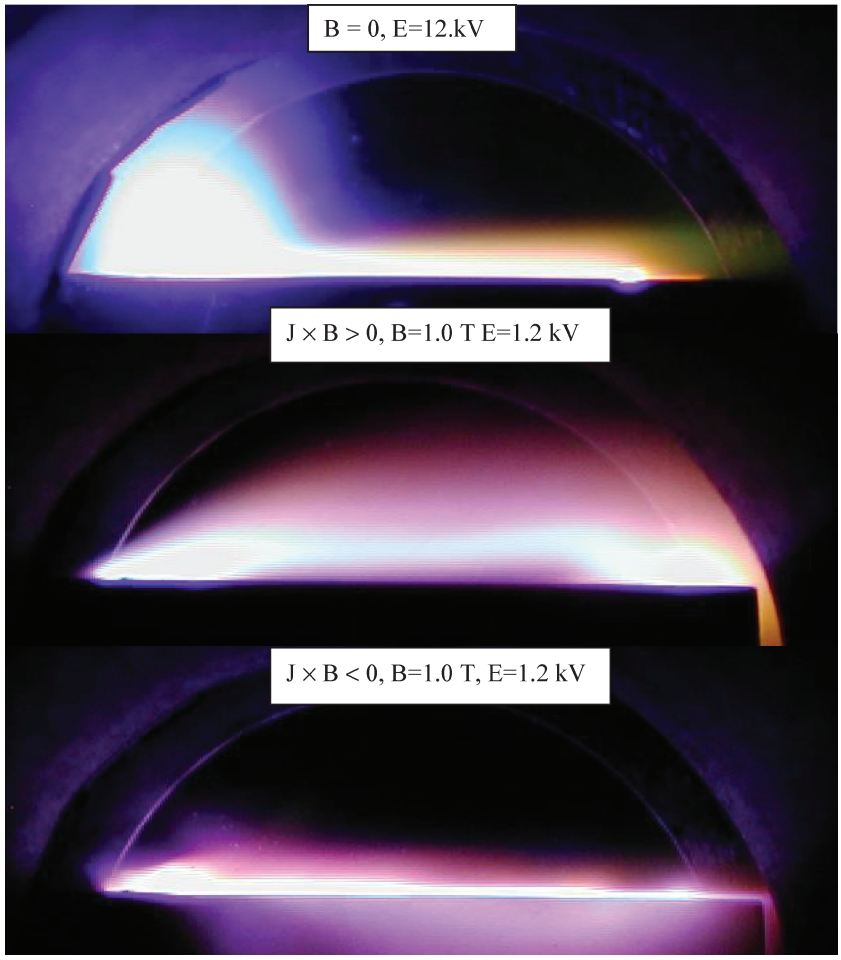

Fig. 19 Magnetoaerodynamic interactions: $Po = 370$ torr, $To = 300$ K, and $E = 1.2$ kV.

interaction together with a nonlinear aerodynamic amplifier is equally applicable to creating a virtual variable geometry, hypersonic inlet for an airbreathing propulsion system. In principle, a series of segmented glow discharge electrodes in a hypersonic inlet can generate a nearly isentropic compression that is difficult to achieve by a purely aerodynamic mechanism alone.[1,8]

IX. Conclusions

A low-density plasma channel for basic research has been successfully developed for simulating the flight environment up to 50,000 m (150,000 ft) at a flight Mach number of 5. The weakly ionized gas created by dc discharge alone is characterized by an electron temperature about 10,000 K, an electron density up to $2 \times 10^{12}/\text{cm}^3$, and an electric conductivity of 2 mho/m. A steady-state solenoid has been integrated into the experimental facility. The experimental data confirmed that the maximum Stuart number per unit length $\sigma B^2/\rho u$ is around 1.5 per meter.

Significant progress has been made in research for diagnostic tools for determining intrinsic properties of a weakly ionized gas including optical spectroscopy, microwave devices, and Langmuir probes. A set of benchmark experimental data for computational magnetoaerodynamics has been obtained from this new facility.

A magnetoaerodynamic interaction has been demonstrated in this new hypersonic plasma channel. In spite of the low electron number density generated by a direct-current glow discharge, a significant induced pressure is derived from the electromagnetic effect and amplified by the ensuing viscous-inviscid interaction. This simple concept can introduce an effective plasma actuator for hypersonic flow control.

Acknowledgments

The research team is grateful for the vision and leadership of Col. David Walker when he led the Air Vehicles Directorate, U.S. Air Force Research Laboratory. This magnetoaerodynamic facility would not have come to fruition without his support and encouragement. The sponsorship by J. Schmisseur of the Air Force Office of Scientific Research is also deeply appreciated. The invaluable contributions by Juan Martinez of the U.S. Air Force Research Laboratory and Sean Henderson and Andrew Kurpik of Wright State University are duly acknowledged. The computing resource was supported by the Computational Science Center of Excellence, U.S. Air Force Research Laboratory at Wright–Patterson Air Force Base.

References

[1]Resler, E. L., Jr., and Sears, W. R., "The Prospects for Magneto-Aerodynamics," *Journal of Aeronautical Science*, Vol. 25, No. 4, 1958, pp. 235–245, 258.

[2]Resler, E. L., Jr., and Sears, W. R., "The Prospects for Magneto-Aerodynamics—Corrections and Addition," *Journal of Aeronautical Science*, Vol. 26, No. 5, 1959, p. 318.

[3]Roth, J. R., Sherman, D. M., and Wilkinson, S. P., "Electrohydrodynamic Flow Control with a Glow-Discharge Surface Plasma," *AIAA Journal*, Vol. 38, No. 7, 2000, pp. 1166–1172.

[4]Howatson, A. M., *An Introduction to Gas Discharge*, 2nd ed., Pergamon, Oxford, 1975, pp. 51–83.

[5]Shang, J. S., Ganguly, B., Umstattd, R., Hayes, J., Arman, M., and Bletzinger, P., "Developing a Facility for Magneto-Aerodynamics Experiments," *Journal of Aircraft*, Vol. 17, No. 6, 2000, pp. 1065–1072.

[6]Miles, R. B., "Flow Control by Energy Addition into High-Speed Air," AIAA Paper 2000-2324, June 2000.

[7]White, A. R., Palm, P., Plonjes, E., Subramaniam, V. V., and Adamovich, I. V., "Effect of Electron Density on Shock Wave Propagation in Optically Pumped Plasma," AIAA Paper 2001-3058, June 2001.

[8]Shang, J. S., "Historical Perspective of Magneto-Fluid-Dynamics," Lecture Series on Introduction to Magneto-Fluid-Dynamics for Aerospace Applications, Paper 2004-01, Oct. 2003.

[9]Dahm, F. J., "Air Condensation in a Hypersonic Wind Tunnel," *AIAA Journal*, Vol. 1, No. 5, 1963, pp. 1043–1046.

[10]Estevadeerdal, J., Gogineui, S., Kimmel, R. L., and Hayes, J. R., "Schlieren Imaging in Hypersonic Plasma," AIAA Paper 2004-1139, Jan. 2004.

[11]Kimmel, R. L., Hayes, J. R., Menart, J. A., Shang, J., and Henderson, S., "Measurement of a Transverse DC Discharge in a Mach 5 Flow," AIAA Paper 2003-4165, June 2003.

[12]Shang, J. S., Hayes, J., Harris, S., Umstattd, R., and Ganguly, B., "Experimental Simulation of Magneto-Aerodynamic Hypersonics," AIAA Paper 2000-2258, June 2000.

[13]Hertzberg, G., *Molecular Spectra and Molecular Structure. 1. Spectra of Diatomic Molecules*, Van Nostrand, New York, 1950, pp. 127–253.

[14]Menart, J., Shang, J., and Hayes, J., "Development of a Langmuir Probe for Plasma Diagnostic Work in High Speed Flow," AIAA Paper 2001-2804, June 2001.

[15]Plonjes, E., Palm, P., Adamovich, I. V., and Rich, J. W., "Characteristic of Electron-Mediated Vibration Electronic (V-E) Energy Transfer in Optically Pumped Plasma Using Langmuir Probe Measurements," AIAA Paper 2002-2243, 2002.

[16]Menart, J. A., Shang, J. S., Henderson, S., Kurpik, A., Kimmel, R., and Hayes, J., "Survey of Plasma Generated in a Mach 5 Wind Tunnel," AIAA Paper 2003-1194, Jan. 2003.

[17]Menart, J. A., and Shang, J. S., "Data Reduction Analysis for Cylindrical, Double Langmuir Probes Operating in Collisionless to Collisional, Quiescent Plasma," AIAA Paper 2003-0136, Jan. 2003.

[18]Heald, M. A., and Wharton, C. B., *Plasma Diagnostic with Microwaves*, Wiley, New York, 1965, pp. 117–154.

[19]Strang, W. Z., Tomaro, R. F., and Grismer, M., "The Defining Methods of Cobalt_{60}: A Parallel, Implicit, Unstructured Euler/Navier–Stokes Flow Solver," AIAA Paper 99-0786, Jan. 1999.

[20]Gottlieb, J. J., and Groth, C. P. T., "Assessment of Riemann Solvers for Unsteady One-Dimensional Inviscid Flows of Perfect Gases," *Journal of Computational Physics*, Vol. 78, No. 2, 1988, pp. 437–458.

[21]Grismer, M. J., Strang, W. Z., Tomaro, R. F., and Witzman, F. C., "Cobalt: A Parallel, Implicit, Unstructured Euler/Navier–Stokes Solver," *Advances in Engineering Software*, Vol. 29, April–July 1998, pp. 365–373.

[22]Spalart, P. R., and Allmaras, S. R., "A One-Equation Turbulent Model for Aerodynamic Flows," AIAA Paper 92-0439, Jan. 1992.

[23]Shang, J. S., and Surzhikov, S. T., "Magneto-Aerodynamics Interaction for Hypersonic Flow Control," AIAA Paper 2004-0508, Jan. 2004.

[24]Kimmel, R., Hayes, J., Menart, J., and Shang, J. S., "Effect of Surface Plasma Discharges on Boundary Layer at Mach 5," AIAA Paper 2004-0509, Jan. 2004.

[25]Menart, J., Shang, J. S., Kimmel, R., and Hayes, J., "Effects of Magnetic Fields on Plasma Generated in a Mach 5 Wind Tunnel," AIAA Paper 2003-4165, June 2003.

[26]Hayes, W., and Probstein, R., *Hypersonic Flow Theory*, Academic Press, New York, 1959, pp. 333–374.

A. Ketsdever
Associate Editor

Color reproductions courtesy of U.S. Air Force Research Laboratory.